A genome-scale metabolic model of a pathosystem sheds new light on bacterial wilt

Léo Gerlin[1,2], Stéphane Genin[1], Caroline Baroukh[1]*

[1]Univ Toulouse, INRAE, CNRS, LIPME, Castanet-Tolosan, France

[2]INRAE, INSA Lyon, BF2I, UMR203, 69621 Villeurbanne, France

*Corresponding author: caroline.baroukh@inrae.fr

ORCID: 0000-0002-1041-1730 (CB)

ORCID: 0000-0003-2498-2400 (SG)

ORCID: 0000-0002-1398-2790 (LG)

Keywords

Genome-scale metabolic model; plant-pathogen interaction; tomato; *Ralstonia solanacearum;* putrescine

Summary

• During plant infection, complex metabolic interactions occurs between host and pathogen, including a genuine competition for resources. While the pathogen exploits host nutrients to support its growth and virulence, the plant attempts to restrict pathogen multiplication by limiting nutrient availability or producing antimicrobial compounds.

• To unravel these trophic interactions, we constructed a genome-scale metabolic model of a complete pathosystem by integrating a multi-organ metabolic model of the plant, a pathogen metabolic model, quantitative measurements, and a mathematical framework based on sequential flux balance analyses (FBAs). This strategy was applied to the *Ralstonia pseudosolanacearum*-tomato system.

• For the first time, quantitative fluxes of matter occurring during a plant infection were predicted. The model shows that (i) plant photosynthetic capacity is a stronger constraint than mineral availability for bacterial proliferation, (ii) infection-induced reduction of plant transpiration limits and ultimately halts first plant growth, then pathogen expansion, (iii) stem resource hijacking can enhance bacterial growth but remains secondary, and (iv) pathogen-excreted putrescine is likely reused for the plant's needs.

• This study delivers the first holistic and quantitative representation of trophic interactions within a plant-pathogen system and highlights the central importance of water flow when the infectious agent is a fast-growing, xylem-colonizing bacterium.

Introduction

Metabolism is a crucial parameter at the center of interactions between plants and pathogens. Indeed, during host infection, pathogens must efficiently find resources in hostile (and sometimes nutrient-poor) environments to sustain both their growth and virulence (Abu Kwaik & Bumann, 2013). This implies a trade-off for the infecting pathogen, which must balance its carbon and energy expenditure between two objectives: on one hand, limiting plant defense and hijacking plant resources, and on the other hand, supporting its own multiplication and proliferation (Berger et al., 2007). On the plant side, a similar trade-off exists where the plant must distribute resources between maintenance/growth (to ensure reproduction) and immunity, while coping with an increasing infecting population that affects its physiology (Herms & Mattson, 1992; Walters & Heil, 2007). Understanding the complex metabolic interactions occurring between the plant and the pathogen is essential for gaining a holistic view of the infection process. In particular, this knowledge could help to clarify (i) what drives the altered plant phenotype during infection (e.g., growth arrest), (ii) which environmental factors (light, minerals, etc.) limit pathogen growth and population density, (iii) whether the pathogen is able to reprogram the host to allocate nutrients for its own benefit, as *Agrobacterium tumefaciens* does with opines (Zupan et al., 2000), and (iv) how plant metabolic pathways are affected by the presence of the pathogen, especially if the pathogen excretes metabolites. However, the use of a simple metabolomic comparison between infected and non-infected plants is not enough to answer these biological questions, in particular because pathogen metabolism is nearly indistinguishable from plant metabolism, except for very specific metabolites, and metabolism results from the dynamic interplay of multiple synthesis and degradation processes. To better tackle this interaction, a systemic and computational approach is necessary. Ideally, this approach should be quantitative, since only by assigning numerical values can one capture orders of magnitude, thresholds, and trade-offs that would otherwise remain invisible in purely qualitative reasoning.

To this end, we propose in this study to use genome-scale metabolic models (GSMM). GSMMs integrate the metabolic potential of an organism of interest, encompassing thousands of metabolic reactions based on genomics, physiological and biochemical evidences. These models generate quantitative estimations of how matter flows through the biological system under investigation (Gu et al., 2019) as well as

phenotypic parameters such as growth. GSMMs have repeatedly proven to be pertinent tools for unraveling complex metabolism, making them suitable for elucidating plant - pathogen metabolic interactions (Gerlin, Frainay, et al., 2021).

Recently, genome-scale metabolic modeling has been applied to the plant – pathogen system of tomato and *Phytophthora infestans* (Rodenburg et al., 2019). It allowed to identify potential pathogen's targets and plant pathways to engineer in order to block the infection process (Gerlin, Frainay, et al., 2021) but the model developed only provided qualitative insights by exploiting connectivity and topology. It also did not predict the effect of the presence of the pathogen on plant physiology.

A quantitative model of the plant – mutualist symbiont system *Medicago truncatula* - *Sinorhizobium meliloti* has also been recently developed (Pfau et al., 2018; diCenzo et al., 2020). Yet modeling a pathogenic interaction, as compared to a mutualistic one, raises additional methodological questions: i) the choice of the objective function (i.e. the flux(es) to minimize/maximize) in an antagonistic relationship, given that the modeling approach assumes an optimal behavior of the biological system; ii) the need for extensive data acquisition, including the plant/pathogen ratio, growth rates, and metabolites available for the pathogen. These considerations are crucial for developing accurate, meaningful and quantitative models of plant-pathogen interactions.

In this study, we constructed the first quantitative genome-scale metabolic model of a plant–pathogen interaction. For our model pathosystem, we used *Ralstonia pseudosolanacearum* GMI1000 and its natural host, the tomato plant. *R. pseudosolanacearum* is a soil-borne beta-Proteobacterium that enters plants through roots to reach the vascular tissues. The pathogen is then able to reach aerial parts, and proliferate dramatically in xylem vessels, which are typically considered nutrient-poor environments (De La Fuente et al., 2022). Bacterial density has been identified as the cause of xylem vessel clogging (Ingel, Caldwell, Duong, Parkinson, McCulloh, Iyer-Pascuzzi, McElrone, & Lowe-Power, 2022), leading to lethal wilting symptoms. A progressive growth arrest and transpiration decline of the plant has also been observed (Gerlin, Escourrou, et al., 2021). *R. pseudosolanacearum* has been extensively studied for its virulence factors (Vailleau & Genin, 2023) and has gained growing attention for the metabolic aspects of its lifestyle (Peyraud et al., 2016; Lowe-Power et al., 2018; Lowe-Power et al., 2018; Peyraud et al., 2018; Hamilton et al., 2021; Gerlin, Escourrou, et al., 2021). It was among the first plant pathogens having a high-quality GSMM

104 (Peyraud et al., 2016). GSMMs for the tomato plant, *R. pseudosolanacearum*'s natural
105 host, were also developed (Gerlin, Frainay, et al., 2021): a cell genome-scale metabolic
106 model was originally published in 2016 (Yuan et al., 2016) and a genome-scale multi-
107 organ metabolic model, with particular emphasis on xylem vessels (where *R.*
108 *pseudosolanacearum* is most metabolically active), was recently published (Gerlin et
109 al., 2022). A core metabolic model of tomato stem in the context of a fungal infection
110 has also been developed (Lacrampe et al., 2024).

111 The quantitative genome-scale metabolic model developed in this study was named
112 VIRION for VIrtual Ralstonia-tomato plant interactION. It was based on the multi-organ
113 metabolic model of the tomato plant, representing different plant organs during
114 vegetative growth (leaf, stem, root with xylem and phloem as exchange
115 compartments), combined with *R. pseudosolanacearum* model represented as an
116 additional compartment connected to the xylem. To accurately simulate the
117 antagonistic interaction between the plant and the pathogen, we employed a set of
118 sequential Flux Balance Analyses (FBAs). To be more accurate, VIRION also
119 integrates a comprehensive set of physiological and metabolic data: i) tomato
120 vegetative growth (organ ratio, growth rates, xylem metabolites), ii) tomato infection by
121 *R. pseudosolanacearum* (plant/pathogen ratios, impacts of infection on physiology),
122 and iii) *R. pseudosolanacearum* physiology and metabolic capacities (growth rates,
123 assimilation and excretion capacities on xylem metabolites).

124 The model only focused on the trophic aspect of metabolism. It did not account for the
125 plant's immune response or the pathogen's virulence, as modeling such phenomena
126 is highly challenging and requires alternative approaches such as dynamic gene
127 regulatory networks or functional association networks (e.g., immunity-related
128 metabolomic measurements) that are not available for our pathosystem. Moreover, the
129 present study addressed an infection stage that, in the case of *Ralstonia*, corresponds
130 to intense multiplication within plant tissues, and thus likely occurs once most of the
131 immune defenses have already been overcome (Gerlin, Escourrou, et al., 2021;
132 Baroukh et al., 2025). At this stage, trophic interactions are therefore expected to be
133 predominant. In addition, this stage of the interaction has received little attention so
134 far, whereas numerous studies have focused on early plant immunity, such as
135 perception and signaling (DeFalco & Zipfel, 2021; Jian et al., 2023).

136 The model enables to generate quantitative estimation of the growth capacities of *R.*
137 *pseudosolanacearum in planta* at different stages of the disease, as well as the
138 pathogen's impact on plant growth and metabolism. We used the model to analyze
139 factors causing the infected plant to cease growth and those limiting bacterial growth.
140 Finally, we also investigated potential hijacking of stem resources during the disease,
141 and the fate of the bacterial excreted putrescine in the plant.

142 Results

143 Modeling an antagonist plant-pathogen interaction using a multi-
144 compartment metabolic model and sequential Flux Balance
145 Analyses

146 To model the metabolic interaction between *R. pseudosolanacearum* and the tomato
147 plant, we represented the system as four metabolic compartments corresponding to
148 the main metabolic roles of the plant (leaf, stem, root) and the pathogen. Metabolites
149 can be exchanged between these compartments through xylem and phloem (Figure
150 1A). Each of these four compartments was represented as a genome-scale metabolic
151 model: iRP1476 for the pathogen (Peyraud et al., 2016) and Sl2183 for the plant
152 compartments (Gerlin et al., 2022) (Figure 1B), with minor modifications as reported in
153 the Methods section. As in Gerlin et al. (2022), the physiological roles of each
154 compartment (described in Figure 1A) were implemented as FBA constraints (Figure
155 1B). In brief: i) minerals and water can enter the system only through the root and are
156 transported to the upper parts of the plant and to the pathogen exclusively via xylem,
157 ii) photons are assimilated in both the leaf and the stem, with higher efficiency in the
158 leaf, iii) the carboxylase/oxygenase activity of the Rubisco was constrained to
159 experimentally measured values. For a complete description and justification of these
160 constraints, readers are referred to Gerlin et al. (2022).

161 FBA is an approach based on an optimization problem (typically formulated as linear
162 programming), in which one or several objective reactions are maximized or minimized
163 to compute metabolic fluxes (Orth et al., 2010). Usually, when modeling ecosystems,
164 the organisms composing the system are assumed to collectively maximize global
165 biomass (diCenzo et al., 2020). However, this assumption is not appropriate for our
166 antagonistic system, in which the pathogen grows at the expense of the plant, leading
167 to decoupled growth dynamics between the two partners. Moreover, in our system, the

168 metabolic composition of xylem sap is severely altered upon bacterial infection,
169 particularly at high bacterial densities (Gerlin, Escourrou, et al., 2021), thereby
170 challenging the quasi-steady state assumption (QSSA). To model this antagonistic
171 relationship, we employed a system of sequential FBAs (Figure 1C). In this approach,
172 an initial FBA determines one or several optimal flux(es), which are subsequently
173 reinjected into the next FBA as additional constraints. A total of four successive FBAs
174 were performed for each bacterial density to predict both bacterial and plant
175 metabolism during the interaction. This four-step FBA workflow was repeated for
176 several bacterial densities representative of those observed *in planta* (Gerlin,
177 Escourrou, et al., 2021). Bacterial density was accounted for by adjusting the
178 stoichiometric coefficients of the exchange reactions between the xylem and the
179 pathogen for each density (see Methods for details).

180 The sequential 4-FBA approach consisted of the four following steps:

181 FBA 1: Estimation of the requirements of a healthy plant in terms of photons, nitrogen
182 and other minerals necessary for an optimal growth of the leaf, stem and root.

183 FBA 2: Estimation of pathogen growth while constraining plant photon and mineral
184 inputs to the levels obtained in FBA 1. This ensured that resource consumption did not
185 exceed that of a healthy plant. Photon constraints were always applied, whereas
186 mineral constraints were optional. In addition, the transpiration flow – known to be
187 significantly reduced after pathogen inoculation (Gerlin, Escourrou, et al., 2021) and
188 influence xylem exchanges - could be constrained at this step (see Methods for
189 details).

190 FBA 3: Estimation of leaf and stem growth rates given the pathogen growth determined
191 in FBA 2. In both FBA 2 and FBA 3, the root growth rate was fixed to experimentally
192 observed values, since root growth is minimally affected by xylem colonization
193 according to experimental data on infected tomato plants (Gerlin, Escourrou, et al.,
194 2021).

195 FBA 4: Estimation of metabolic fluxes in the pathosystem under a parsimonious
196 enzyme usage constraint. This final simulation yielded the flux distribution for a given
197 bacterial density.

198 These 4 FBAs were performed for bacterial densities ranging from 10^6 to 10^{12} Colony
199 Forming Unit per gram of plant Fresh Weight ($CFU.g^{-1}$ FW), which are bacterial
200 densities typically measured in the plant during an infection cycle (Gerlin, Escourrou,

et al., 2021). The simulation results – including plant and pathogen growth rates and the composition of xylem fluxes upon infection - were compared with experimentally observed behaviors to validate the model and gain insights into the pathosystem.

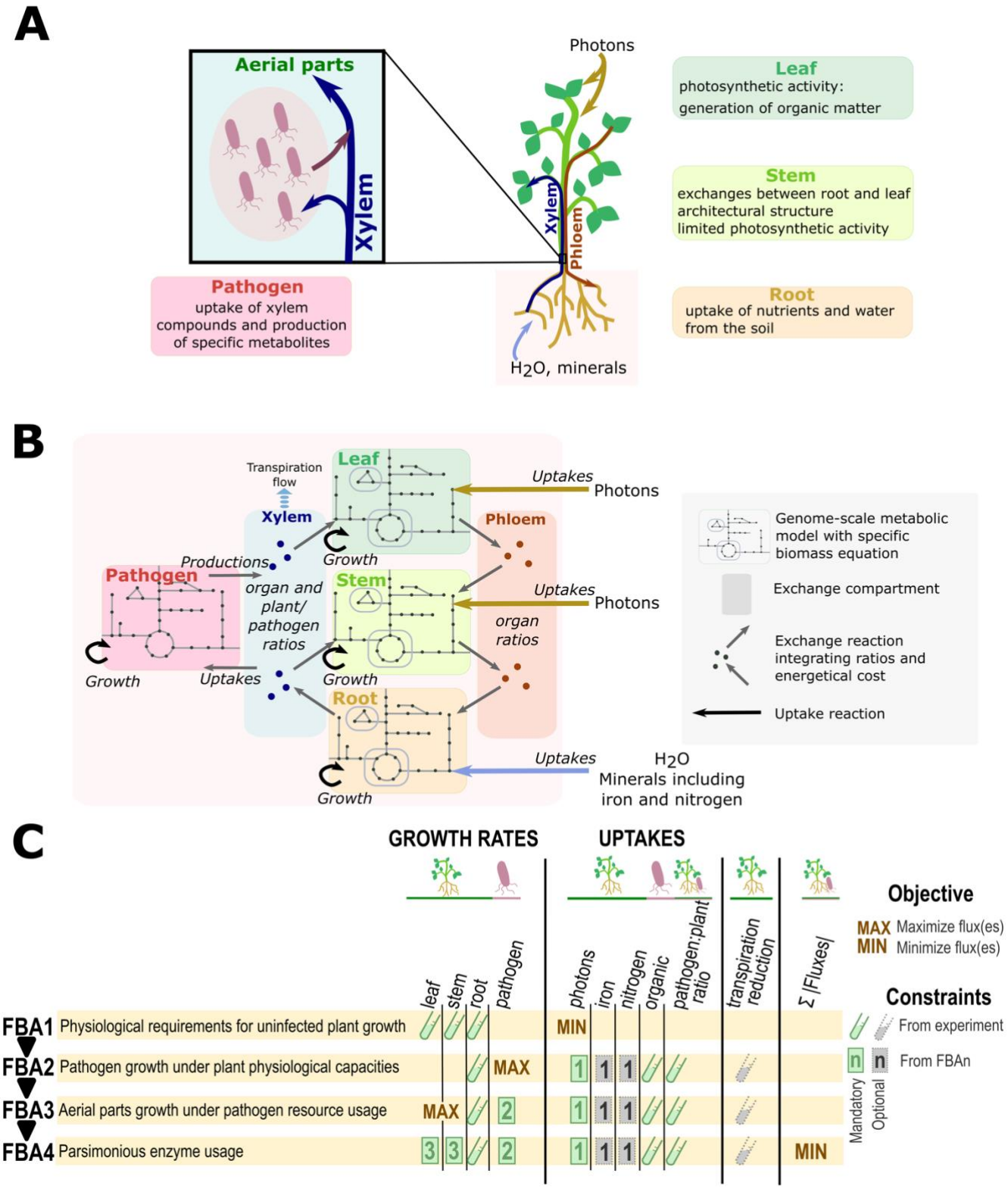

Figure 1: Schematic representation of the metabolic model VIRION

206 A. The main components of the system modeled in this study. Leaf, stem, root and the
207 pathogen are each represented by a genome-scale metabolic model. Xylem and
208 phloem are exchange compartments. Inputs of the system are photons, connected to
209 leaf and stem, and water and minerals, connected through the root.

210 B. Schematic representation of the multi-compartment model and quantitative
211 approach used in this study. Arrows represent relationships between the different
212 organs and the possible quantitative constraints which can be set in the model (growth,
213 uptakes, exchanges, transpiration flow).

214 C. Sequential Flux Balance Analyses (FBAs). Schematic representation of the different
215 FBAs solved in a sequential approach to obtain a phenotype prediction of the
216 pathosystem (growth rate of plant organs and pathogen) as well as fluxes of matter.
217 The constraints from experiments are detailed in Supplementary Table 1.

218 Identifying metabolic bottlenecks during the plant – pathogen 219 interaction

220 We used the VIRION model to assess which plant environmental factors - light,
221 nitrogen, iron or water - constrained the plant-pathogen interaction. The analysis
222 considered these factors individually and in combination (Figure 2A). Because infected
223 plants displayed reduced leaf area compared to healthy ones (Gerlin, Escourrou, et
224 al., 2021), light constraint was treated as mandatory: an infected plant cannot absorb
225 more photons than a healthy plant. While other minerals could be studied, our study
226 focused on nitrogen and iron. Nitrogen source affects the concentration of xylem
227 organic metabolites in tomato (Bialczyk et al., 2004), and both nitrogen and iron were
228 suggested to influence the switch to virulence in *R. pseudosolanacearum* (Bhatt &
229 Denny, 2004; Dalsing & Allen, 2014; Dalsing et al., 2015). Light, nitrogen and iron were
230 constrained on their respective uptake rates from FBA 2. The imposed bounds
231 corresponded to the rates computed in FBA 1 (minimization of plant photons for a
232 healthy tomato plant, Figure 1C). Transpiration was also optionally limited by
233 constraining the upper bound of root to xylem transport fluxes, based on a previously
234 established linear relationship between *in planta* bacterial density and transpiration
235 reduction (Gerlin, Escourrou, et al., 2021) (see Methods for further details).

236 When light is the sole limiting factor (Figure 2), thereby constraining photosynthesis
237 and organic carbon production, *R. pseudosolanacearum* grows at its maximal rate up

238 to a density of $10^{9.7}$ CFU.g^{-1} FW (Figure 2B). Beyond this threshold, bacterial growth
239 declines sharply, falling below 0.05 h^{-1} once densities exceed $10^{10.6}$ CFU.g^{-1} FW.
240 These results indicate that if Ralstonia relies exclusively on biotrophic growth sustained
241 by xylem sap metabolites, the plant cannot support bacterial proliferation beyond
242 roughly 10^{10} CFU.g^{-1} FW. Analysis of the simulated substrate uptake fluxes reveals
243 that glutamine is the primary carbon source sustaining Ralstonia growth (Figure 2D).
244 Glutamine uptake remains high up to approximately 10^{10}CFU.g^{-1} FW, beyond which it
245 becomes limiting – first for the growth of the plant's aerial tissues, and subsequently
246 for Ralstonia. This limitation is temporarily alleviated by glucose uptake, a secondary
247 carbon source that is co-consumed with glutamine. However, at slightly higher
248 bacterial densities ($10^{10.25}$ CFU.g^{-1} FW), the maximal glucose uptake flux in the xylem
249 is also reached, further constraining bacterial growth. These simulation results are
250 consistent with experimental observations: *in planta* analyses and *in vitro* assays have
251 identified glutamine as the principal carbon source of *R. pseudosolanacearum* in
252 tomato xylem sap (Baroukh et al., 2022; Gerlin, Escourrou, et al., 2021; Baroukh et al.,
253 2025). While glucose can moderately support bacterial proliferation, it has been shown
254 to play only an accessory role (Baroukh et al., 2022, 2025; Gerlin, Escourrou, et al.,
255 2021; Hamilton et al., 2021).

256 However, plant growth capacities were overestimated by the simulations results:
257 optimal leaf and stem growth were maintained in silico up to a bacterial density of $10^{8.5}$
258 CFU.g^{-1} FW (Figure 2C), whereas strong growth inhibition was experimentally
259 observed between 10^6 and 10^8 CFU.g^{-1} FW (Gerlin, Escourrou, et al., 2021). This
260 discrepancy indicates that additional factors contribute to plant growth arrest. When
261 mineral constraints—specifically iron and nitrogen—were applied, either separately or
262 together, the simulation outcomes were similar to those obtained under light limitation
263 alone (Figure 2). Nitrogen and iron therefore appeared to be less stringent bottlenecks
264 than light. In contrast, limiting transpiration flow produced distinct results, with a decline
265 in both plant and Ralstonia growth rates occurring at lower bacterial densities (Figure
266 2). Indeed, from approximately 10^7 CFU.g^{-1} FW, reduced transpiration limited the
267 availability of xylem sap nutrients for both the bacterium and the aerial tissues.
268 Because the model prioritizes Ralstonia growth at the expense of that of the plant, an
269 immediate effect on plant development was observed (Figure 2C).

At higher bacterial densities, xylem fluxes became insufficient to sustain rapid Ralstonia growth, resulting in an intermediate growth rate (Figure 2B) before a complete decline beyond 10^9 CFU.g^{-1} FW. Interestingly, glutamine remained abundant enough to satisfy the maximal uptake rate of *R. pseudosolanacearum* (Figure 2D), but other metabolites present at low concentrations in the xylem—such as glucose (Figure 2F), sucrose, and amino acids (Supplementary Figure 1)—were no longer assimilated or only at reduced rates, explaining the intermediate growth phase observed. Above 10^9 CFU.g^{-1} FW, glutamine availability also became limiting, severely impairing bacterial growth and rapidly leading to growth arrest. These findings are consistent with experimental data, which report maximal bacterial densities around 10^9 CFU.g^{-1} FW (Gerlin, Escourrou, et al., 2021). They also align with predictions from a recently developed macroscopic model of *R. pseudosolanacearum* growth in planta (Baroukh et al., 2025).

Finally, adding nitrogen and iron limitations to the model—already constrained by photon availability and transpiration—did not markedly alter the simulated progression of the disease (Figure 2B–G). This result suggests that the decline in plant transpiration, which reduces xylem fluxes, exerts the strongest influence on both plant and pathogen metabolic capacities. Transpiration decline therefore appears to be the most probable mechanism underlying plant growth arrest, pathogen growth arrest, and the establishment of maximal bacterial density. In contrast, limitations in nitrogen, iron, or carbon (via photon limitation) do not seem to represent the primary drivers of these experimental observations.

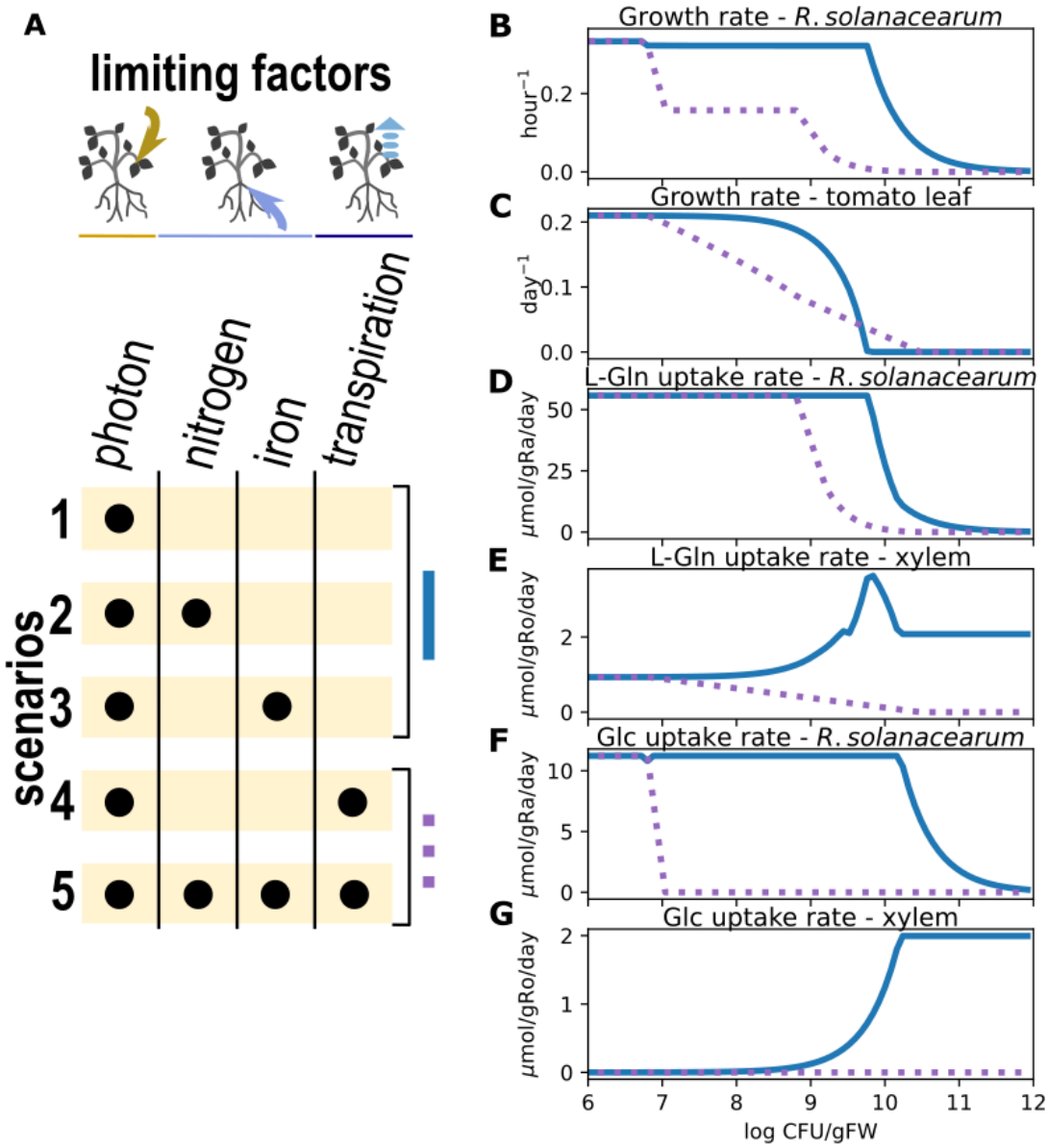

Figure 2: Effect of plant environmental conditions on growth and metabolic exchanges in the pathosystem. A. Simulation scenarios in which different plant environmental conditions were constrained at the FBA 2 step during sequential FBAs. The upper bounds of photons, nitrogen and iron were set to the values obtained from FBA 1. Transpiration constraint was implemented as constraints on the upper bound of fluxes from root to xylem using a linear relationship computed using the experimental values of Gerlin et al. (Gerlin, Escourrou, et al., 2021). B. to G. Effects of plant environmental conditions on growth and metabolic exchanges for bacterial densities ranging from 10^6 to 10^{12} CFU.g^{-1} FW. gRa: dry weight grams of *R. pseudosolanacearum,* gRo: dry weight grams of root, L-Gln: L-Glutamine, Glc: D-glucose, CFU: colony forming units, FW: fresh weight.

Assessing if hijacking tomato stem resources is a good pathogen strategy

In the previous simulations, the contribution of stem metabolism to xylem sap was forbidden, as no flux from the stem to the xylem was predicted for a healthy plant (Gerlin et al., 2022). However, it can be hypothesized that such fluxes might occur in an infected tomato plant, potentially contributing to pathogen nutrition if the bacterium employs a host resource hijacking strategy. This idea aligns with the hypothesis that certain type III secretion effectors of *R. pseudosolanacearum* can modify plant metabolism (Landry et al., 2020; Macho, 2016).

We re-modeled scenario #5 from the previous section (where photons, nitrogen, iron, transpiration limitations were applied, Figure 2A), this time allowing nutrient export from the stem to the xylem, creating scenario #6 (Figure 3A). Simulation results indicated that permitting the stem to enrich xylem sap had only a slight effect on tomato leaf growth (Figure 3C). In contrast, a more pronounced effect was observed on pathogen growth (Figure 3B): *Ralstonia* could maintain a maximal growth rate up to $10^{9.2}$ CFU.g^{-1} FW, compared to 10^{7} CFU.g^{-1} FW in scenario #5 (Figure 3B).

This enhanced capacity for growth at higher bacterial densities was due to the enrichment of xylem sap in glucose, sucrose, and amino acids, facilitated by the stem's contribution (Figure 3D; Supplementary Figure 1). Nutrients from the stem thus partially counterbalanced the effect of reduced transpiration and allowed *R. pseudosolanacearum* to reach higher densities. However, the plausibility of such extensive rewiring of stem fluxes by the pathogen is questionable in light of experimental data. Indeed, bacterial population dynamics measured *in planta* (Gerlin et al., 2021) show near-complete cessation of bacterial growth at approximately 10^{9} CFU.g^{-1} FW, aligning more closely with scenario #4 or #5 (without stem resource hijacking) than with scenario #6.

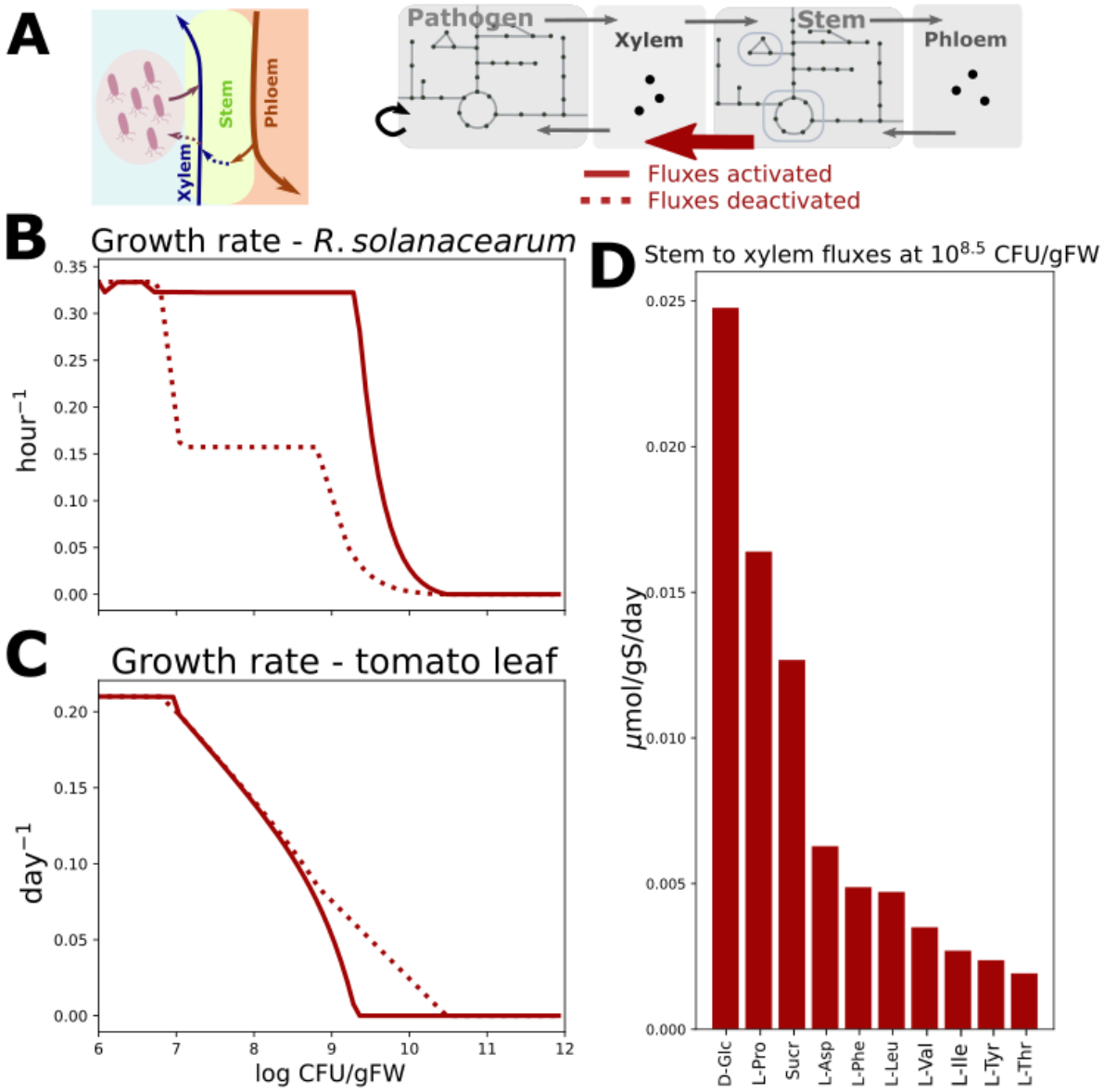

Figure 3: Effect of xylem sap enrichment by the stem on plant growth, pathogen growth and xylem sap composition. A. Schematic representation of the investigated plant fluxes. In scenarios #1 to #5, the stem could not enrich xylem sap. This constraint was lifted to assess its effect on the metabolism of the pathosystem. B. Pathogen growth rate when the stem can (line) or cannot (dotted line) enrich xylem sap. C. Plant growth rate when the stem can (line) or cannot (dotted line) enrich xylem sap. D. Fluxes of matter from stem to xylem when the stem can enrich xylem sap. Fluxes were computed for a bacterial density of $10^{8.5}$ CFU.g^{-1} FW. Fluxes are 0 when stem cannot enrich xylem sap. gS: grams of stem dry weight. D-Glc: D-Glucose, L-Pro: L-Proline, Sucr: sucrose, L-Asp: L-Aspartate, L-Phe: L-Phenylalanine, L-Leu: L-Leucine, L-Val: L-Valine, L-Ile: L-Isoleucine, L-Tyr: L-Tyrosine, L-Thr: L-Threonine.

343 ## The fate of putrescine in the *Ralstonia*-tomato interaction

344 Putrescine fate during plant – *R. pseudosolanacearum* interaction is frequently
345 questioned, as putrescine is abundantly produced by the bacterium *in vitro* and *in*
346 *planta* (Gerlin, Escourrou, et al., 2021; Lowe-Power et al., 2018; Peyraud et al., 2016)
347 and contributes to virulence by accelerating wilt symptoms (Lowe-Power et al., 2018).
348 We analyzed predicted fluxes of putrescine in our model including its production by *R.*
349 *pseudosolanacearum* - calibrated to its experimentally measured excretion rate in a
350 xylem-mimicking medium (Baroukh et al., 2025) - and its assimilation by the plant at
351 low and high bacterial densities ($10^{6.5}$ and $10^{8.5}$ CFU.g^{-1} FW) (Figure 4A).

352 When putrescine is produced by the bacterium from ornithine, a small portion is
353 incorporated into the bacterial biomass, while the majority is exported to xylem
354 (Baroukh et al., 2022, 2025; Peyraud et al., 2016). Subsequently, the plant aerial
355 tissues can assimilate part of this excreted putrescine. Our model predicted that at low
356 bacterial density, all putrescine is converted into 4-aminobutanal and then into gamma-
357 Aminobutyric acid (GABA). The amount of GABA produced from putrescine at this
358 bacterial density is insufficient to meet the stem biomass requirements for GABA,
359 which are supplemented by other reactions producing GABA from glutamate
360 (glutamate decarboxylase, R_GUDC, EC 4.1.1.15). At high bacterial density, GABA
361 production from putrescine exceeds the stem biomass requirements. This excess is
362 accommodated by: i) activation of the GABA shunt pathway allowing incorporation of
363 GABA into TCA cycle via transport into mitochondria (R_4abut_tx_m_) and conversion
364 into succinate-semialdehyde (4-aminobutyrate transaminase, R_ABTArm) in the stem,
365 ii) activation of the pathway enabling conversion of putrescine into GABA and its
366 assimilation into the leaf. Other reactions associated with putrescine degradation such
367 as conversion into N-acetylspermidine (N1-acetylspermidine oxidase, identifier
368 R_RE1537C in the model) or into N-Methylputrescine (Putrescine N-
369 methyltransferase, R_PMT), were not predicted to carry fluxes, because these
370 reactions produce dead-end metabolites not connected to central metabolism.
371 Interestingly, excess putrescine assimilated by the plant via GABA leads to mandatory
372 production of hydrogen peroxide (H_2O_2) (Figure 4B), a key modulator of redox
373 homeostasis (Gerlin, Baroukh, et al., 2021), particularly in the stem. H_2O_2 production
374 follows pathogen growth, peaking at approximately at 10^9 CFU.g^{-1} FW. At higher

375 bacterial densities, the pathogen's limited growth capacity reduces putrescine
376 production flux, thereby decreasing H_2O_2 flux.

377

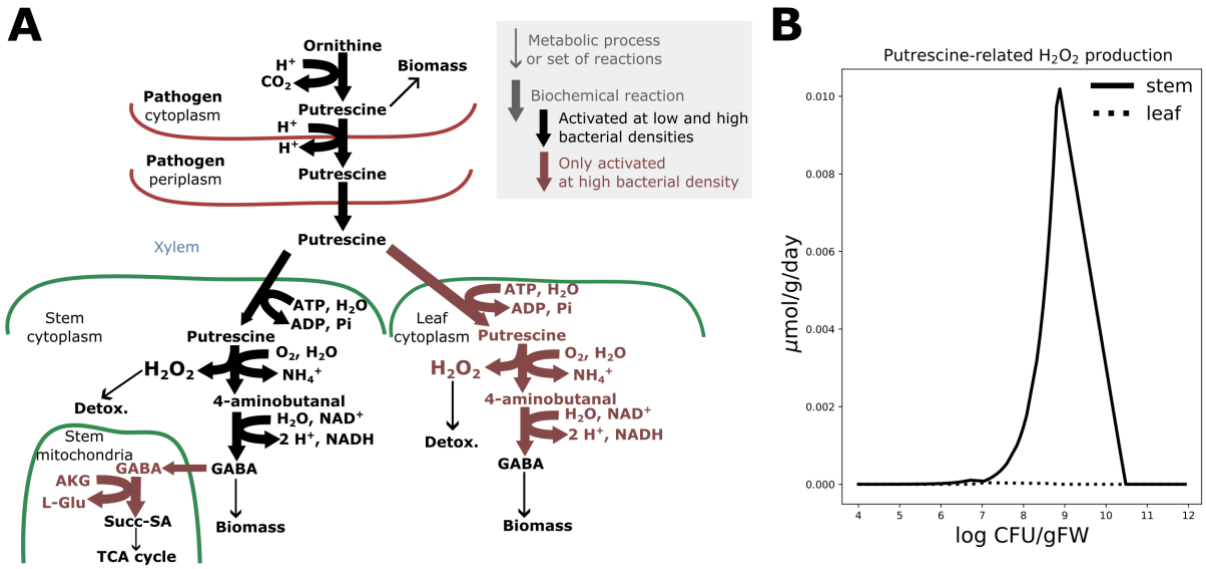

378
379 **Figure 4: Fluxes predictions surrounding putrescine in VIRION.** Only fluxes
380 activated between putrescine production by the pathogen and its assimilation by the
381 plant are represented. In B, g means g of stem (full line) or leaf (dotted line) dry weight.

382

383 # Discussion

384 ## Modeling a plant-pathogen interaction using Flux Balance Analysis

385 FBA is a methodology widely used in the systems biology community because of its
386 simplicity to set up, its capacity to model at the genome-scale level and its relatively
387 low number of parameters to calibrate (Orth et al., 2010). However, this methodology
388 relies on the quasi-steady-state assumption (QSSA), assuming that no internal
389 metabolites of the system accumulate or get depleted, as well as the fact that the
390 system is optimal with respect to an objective (most often assumed to be growth). The
391 difficulty in modeling a plant-pathogen system lies in the fact that the pathogen grows
392 at the expense of the plant, implying antagonistic objectives between the organisms
393 composing the system. Therefore, questions arise regarding the choice of the objective
394 function that should be optimized. In addition, the pathogen might deplete or
395 accumulate some metabolites upon its growth in the plant, which probably challenges
396 the QSSA.

397 As a first approximation to quantitatively model a plant-pathogen interaction, we
398 proposed in this work a methodological framework consisting of solving, for several

399 bacterial densities, 4 sequential FBA models in which each FBA model is constrained
400 by the optimal value of the previously solved FBA. In this methodology, we thus
401 assumed that for each bacterial density inside the plant, the internal metabolites were
402 “at steady-state”. We also assumed that pathogen growth was at the expense of the
403 aerial parts of the plant. Despite these strong hypotheses, VIRION was able to illustrate
404 its relevance by predicting growth rates of the aerial part of the plant and the pathogen
405 close to what was experimentally observed. VIRION also allowed the dissection of
406 novel and previously unquantified aspects of the *R. pseudosolanacearum* – tomato
407 interaction, including the critical of transpiration decline in plant growth arrest, the
408 relative importance of carbon compared to other elements, and the potential
409 contribution of stem resource hijacking.

410 As future directions, the model could be used to study the impact of plant
411 environmental conditions on the plant-pathogen interaction or extended to consider
412 plant defenses via the synthesis of anti-microbial compounds and the resulting
413 bacterial mortality (Zrimec et al., 2025). From a methodological point of view, the QSSA
414 could be slightly relaxed on the metabolites composing the xylem sap, which would
415 allow for more dynamic and relevant modeling of the plant-pathogen interaction.

416 Using mathematical modeling to better understand bacterial wilt 417 disease

418 Since 2016, several mathematical models have been developed to better understand
419 the biology behind bacterial wilt disease. The first model, released in 2016, consisted
420 of a high-quality metabolic network of *R. pseudosolanacearum* simulated in diverse *in*
421 *vitro* environments using FBA (Peyraud et al., 2016). This model allowed measuring
422 the ATP- equivalent cost of EPS synthesis and virulence. This metabolic network was
423 subsequently interfaced with a regulatory network controlling multiple virulence factors
424 and simulated across a broad set of environmental conditions using a discrete logical
425 modeling method (Peyraud et al., 2018). The resulting model revealed that the
426 virulence regulatory network exerts a control of the primary metabolism to promote
427 robustness upon infection.

428 More recently, Baroukh et al. (2024) modeled the *in planta* population dynamics of *R.*
429 *pseudosolanacearum* during tomato infection using a macroscopic modeling
430 framework relying on Monod kinetics. This mathematical model predicted substrate
431 consumption, putrescine production and biomass growth of *R. pseudosolanacearum*.

Unlike previous models, it did not incorporate the metabolic network of *R. pseudosolanacearum* or its regulatory network, nor did it include the plant's metabolic network, which was simply modeled as a continuous environment providing substrate fluxes to the pathogen. Despite these simplifications, the model accurately reproduced experimental observations, including high bacterial densities and the depletion of glutamine and asparagine. Additionally, it estimated key parameters such as the bacterial mortality rate within the plant and the rate at which bacterial putrescine is assimilated by the plant.

In the present study, the metabolic networks of *R. pseudosolanacearum* and the tomato plant were merged, and the resulting model was simulated using sequential FBAs for diverse bacterial densities within the plant. The model demonstrated several key findings: i) the plant's photosynthetic capacity is the most critical factor for bacterial proliferation, ii) a reduction in plant transpiration limits and ultimately stops plant and pathogen growths, iii) hijacking stem resources, potentially through virulence factors, can enhance bacterial growth but is not essential for Ralstonia, and iv) pathogen-excreted putrescine is predicted to be directly reused for plant biomass.

Another metabolic model of a plant-pathogen interaction was recently developed by Rodenburg et al. (2019), representing the *Phytophthora infestans* - tomato leaf pathosystem. This study differs from ours in several key aspects, as it employs a qualitative approach, in contrast to our quantitative methodology. This difference is evident in: i) the *P. infestans* biomass equation, which uses equal stoichiometric coefficients, ii) the absence of mass conversion between plant and pathogen fluxes, iii) the unrestricted uptake of all metabolites from tomato cell cytosol by the pathogen, and iv) the lack of calibration for maximal uptake rates for both *P. infestans* and the plant. Roderburg et al. (2019) also utilized a tomato leaf-centered model, which is substantially less complex than our multi-organ model that incorporates a vascular system, and the impact of *P. infestans* growth on plant metabolism and physiology was not simulated. Indeed, all objective functions in their FBA simulations focused exclusively on pathogen growth, whereas our model considers the interplay between pathogen and plant growth.

In each of the Ralstonia mathematical models developed so far, different modeling approaches have been used, different objects have been modeled, various experimental data have been used for calibration, and distinct biological questions

465 have been addressed. Consequently, each model possesses its own specificity and
466 provides unique insights into the mechanisms at play during bacterial wilt disease.
467 Future directions could involve improving existing models by better representing the
468 plant putrescine degradation pathway. Alternatively, models could be made more
469 complex by considering the spatial aspects of infection and representing the effects of
470 abiotic and biotic conditions of the plant on the pathosystem.

471 Models incorporating plant immunity and its interaction with *R. pseudosolanacearum*
472 virulence factors could also be developed. The first step would be to better represent
473 all the immune-compounds in the metabolic network of the tomato (Zrimec et al., 2025),
474 since the virulence network of *Ralstonia solanacearum* has already been built.
475 However, extensive metabolomics data for both tomato immune metabolites and
476 Ralstonia virulence metabolites will be necessary for calibration to perform quantitative
477 predictions. The second step would be to add the regulatory layer to such model, to
478 better represent triggering of immunity on the plant side and virulence on the pathogen
479 side. This is much more challenging since it requires the hybridization of discrete-
480 regulatory type models with continuous metabolic models (Liu & Bockmayr, 2020;
481 Thuillier et al., 2022). In this study, we focused on a relatively late stage of interaction
482 when the pathogen begins rapid multiplication in host tissues after successful entry
483 and establishment. While the model does not directly account for immunity and
484 virulence mechanisms, it could still successfully evaluate some virulence-related
485 aspects such as the impact of plant resource diversion by the pathogen or the impact
486 of putrescine excretion on the plant H_2O_2 production. VIRION can thus be seen as a
487 starting point for the development of more complex plant-bacteria interaction models
488 that explicitly integrate the interplay between metabolism, immunity and virulence
489 mechanisms.

490 Plant transpiration is the main factor leading to growth arrest of both 491 the host and the pathogen wilt disease

492 VIRION allowed to test and identify which physiological or environmental factors are
493 behind plant and pathogen growth arrests during bacterial wilt disease. First, our
494 simulation results showed that the maximal carbon uptake capacity of the plant
495 (through photosynthesis), not nitrogen or iron, set the maximal plant density of
496 Ralstonia cells achievable (Figure 5). However, we also found that carbon, or any other
497 metabolic bottlenecks such as nitrogen and iron, are insufficient to explain the early

498 arrest of plant growth that was experimentally observed in Gerlin et al. (2021). To
499 explain plant growth arrest, limiting transpiration was necessary. This constraint
500 impacts xylem fluxes and hence access to nutrients for the plant aerial parts and later
501 on the pathogen (Figure 5). Interestingly, at densities where this transpiration-limitation
502 is induced, the plant growth was affected immediately, in agreement with experimental
503 observations, contrary to the bacteria which continued to thrive up to several logs
504 higher. This underlines the pathogen's perfect metabolic adaptation to this challenging
505 environment.

506 Naturally, questions arise on the mechanism responsible of plant transpiration
507 decrease upon *R. pseudosolanacearum* presence in xylem vessels. Physical presence
508 of *Ralstonia* cells could impede xylem flow in itself, but an indirect mechanism such as
509 large bacterial exopolysaccharides excretion could also be responsible by making
510 xylem sap so viscous that it impedes its flow (Ingel, Caldwell, Duong, Parkinson,
511 McCulloh, Iyer-Pascuzzi, McElrone, & Lowe Power, 2022). To discriminate between
512 these hypotheses or others possible mechanisms, further investigation is necessary.

513 Stem resource hijacking, a strategy likely used only minimally by *R.* 514 *pseudosolanacearum* during tomato infection

515 In the literature, xylem sap is commonly described as a nutrient-poor environment that
516 cannot sustain the biotrophic growth of a plant pathogen to high densities (De La
517 Fuente et al., 2022), thereby requiring the bacterium to force the plant to release
518 additional nutrients, such as sugars (Hamilton et al., 2021; MacIntyre et al., 2020).
519 However, VIRION simulations, integrating both xylem concentrations and flow, tend to
520 show that, even with a transpiration limit, a moderate growth rate of *R. solanacearum*
521 can be reached up to 10^9 CFU.g^{-1} FW solely through biotrophic growth, in agreement
522 with experimental observed values (Gerlin, Escourrou, et al., 2021). From 10^{10} CFU.g^{-}
523 ^{1} FW, a growth rate is still present but very close to 0. Thus, xylem sap, when
524 considered as the product of a continuous flow, is not poor and very high bacterial
525 densities can be reached solely through biotrophic growth of the pathogen.

526 We then investigated how resource hijacking could contribute to *R.*
527 *pseudosolanacearum* growth. We confirmed by simulation that this mechanism could
528 theoretically be an effective pathogen strategy to boost its growth and compensate, for
529 example, the effect of transpiration decline, since it allowed the pathogen to have a
530 high growth rate up to 10^{10} CFU.g^{-1} FW. We also confirmed that in the case of stem

531 resource hijacking, this would primarily involve sugars and some amino acids (Figure
532 5). This would explain why Hamilton et al. (2021) reported a slight increase of sugars
533 in infected xylem sap. Nevertheless, we also showed that this mechanism is probably
534 dispensable for *R. pseudosolanacearum* since pathogen growth almost stops at
535 around 10^9 CFU.g^{-1} FW and not 10^{10} CFU.g^{-1} FW (see bacterial population dynamics
536 *in planta* in Gerlin et al. (2021)). This also aligns with the observation that mutants
537 defective in sugar assimilation still fully wilt tomato plants, with a slight delay (Hamilton
538 et al., 2021; Gerlin, Escourrou, et al., 2021). We thus conclude that hijacking plant
539 resources from the stem is not likely to occur in bacterial wilt or, if it does, the quantities
540 of nutrients hijacked are much lower than the maximal quantity that can be theoretically
541 hijacked, as predicted by the model.

542 Reducing the amount of glutamine in the xylem sap, which is the major carbon source
543 for the bacterium, seems to be a better strategy for limiting the growth of *R.*
544 *pseudosolanacearum* in the plant. However, such modifications would likely affect
545 plant metabolism and phenotype even before impacting the pathogen, as our model
546 tends to indicate. Nevertheless, it might be worthwhile to consider how plant variety of
547 managing the plant's environment, such as nutrition or watering, could mitigate xylem
548 sap flow and composition and thus minimize *Ralstonia* growth in the plant.

549 While *R. pseudosolanacearum* appears to favor a fast consumption of resources, as
550 its metabolic and growth capacities outcompete those of the plant, other plant
551 pathogen might not exhibit this behavior but instead favor a reduced growth in xylem
552 vessels. In particular, *Xylella fastidiosa*, although capable of metabolizing various
553 xylem sap components (Gerlin et al., 2020), has very limited growth rates *in vitro* and
554 *in planta*, and is described as adopting a self-limiting behavior (Gerlin et al., 2020;
555 Roper et al., 2019). In these conditions, the plant would be able to dominate the trophic
556 interaction and limit bacterial spread. This suggests that these pathogens would favor
557 a long stay in xylem vessels at low bacterial densities. In this case, a coexistence with
558 the plant takes place in which the bacterium is not competing for resources, and both
559 the plant and the pathogen can remain metabolically active.

560

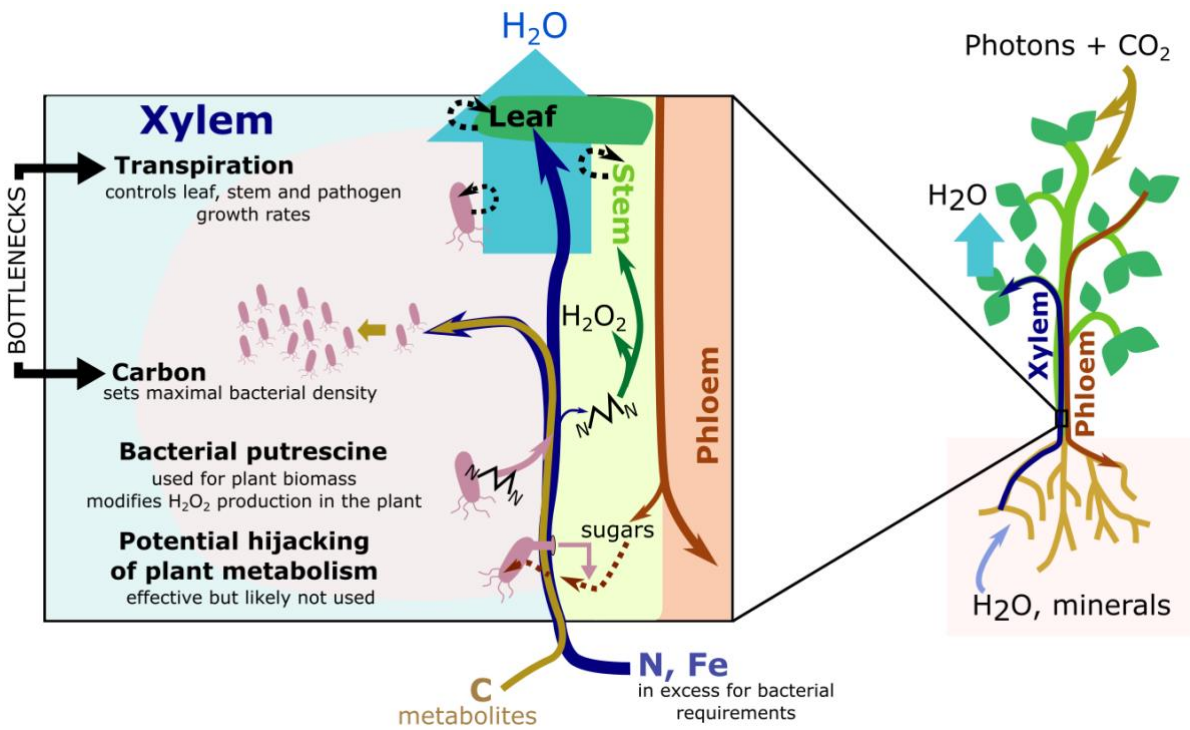

Figure 5: Key metabolic parameters during bacterial wilt at the origin of a successful infection. Decrease in transpiration during infection appears to be the most likely mechanism behind the cessation of plant growth and pathogen growth. Among diverse nutrients, carbon is the most limiting one for bacterial maximal density reachable. The study also showed that, although diverting nutrients from the phloem to the xylem via the stem is an effective strategy for increasing bacterial multiplication in plants, it is poorly used in the case of bacterial wilt. Finally, the effect of bacterial putrescine production on host metabolism was shown to interfere with H_2O_2 synthesis in the plant, likely having an effect on ROS response.

572 # Methods

573 ## Construction of VIRION

574 The cell tomato metabolic model from Gerlin et al., (2022) was used as a starting point.
575 Reactions for iron, manganese, cobalt, molybdenum and zinc assimilation, which were
576 not represented in the initial metabolic model, were added as these metabolites were
577 necessary for predicting *R. pseudosolanacearum* growth using its genome-scale
578 metabolic model (Peyraud et al., 2016). This addition, as well as other changes or
579 improvements on putrescine metabolism and biomass are fully described in
580 Supplementary Text 1.

581 From the single-cell tomato model, a multi-organ model was generated using the same
582 procedure as in Gerlin et al., (2022). Briefly, using an in-house script, the metabolic
583 network was replicated into three metabolic networks representing leaf, stem and root
584 with adequate biomass reaction for each organ. Exchange reactions were added to
585 allow the exchange of metabolites between organs through xylem and phloem,
586 considering weight ratios between the different organs. Xylem represented exchanges
587 between root and aerial parts, while phloem represented exchanges between aerial
588 parts and roots. Stem could exchange in both directions with the phloem. Contrary to
589 our previous multi-organ metabolic model, stem could uptake elements from the xylem
590 but could not provide elements to this compartment, except when mentioned. As in
591 Gerlin et al., (2022), a transport cost was added for each exchange reactions except
592 for water. Different physiological constraints (uptakes of water and minerals by roots
593 only, no photosynthesis for root, limited photosynthesis for stem) were integrated to
594 model the different roles of each organ as in Gerlin et al., (2022).

595 The in-house scripts also merged *R. pseudosolanacearum* metabolic network taken
596 from Peyraud et al. (2016) to the multi-organ network, generating a four-compartment
597 model: leaf, stem, root, pathogen. The boundary metabolites were removed from the
598 metabolic model of *R. pseudosolanacearum*, and external metabolites of the pathogen
599 model were considered as xylem metabolites. To avoid dead-end metabolites, sink
600 reactions were added allowing the exit of *R. pseudosolanacearum* metabolites
601 excreted into the xylem and not present in healthy plant xylem sap. Simulations
602 revealed very few sink reactions were used, and at very low fluxes. In addition,
603 experimental data showed that few metabolites were enriched upon Ralstonia infection

604 in xylem sap (Gerlin, Escourrou, et al., 2021; Lowe-Power et al., 2018). The weight
605 ratio between *R. pseudosolanacearum* and the plant was implemented in the
606 exchange reactions between the xylem and the bacterial periplasm and were modified
607 to represent the different bacterial densities. Conversion of *R. pseudosolanacearum*
608 weight into colony forming unit (CFU) per g of fresh weight (FW) was estimated to
609 follow 1 CFU.g^{-1} stem FW = $1.10 \cdot 10^{-11}$ g bact / 1.52 g stem dry weight, based on: i)
610 OD/CFU and OD/g ratios from Peyraud et al. (2016), ii) fresh weigh/dry weight
611 (FW/DW) from Gerlin et al. (2022), iii) the leaf/stem and stem/root ratio in tomato
612 metabolic model (Gerlin et al., 2022) which impose relative contents of 1.52 g stem
613 DW and 3.37 g leaf DW for 1 g root DW (Supplementary Text 2).

614 Calibration of *R. pseudosolanacearum* metabolic model for growth 615 *in planta*

616 To determine growth, excretion and assimilation capacities of *R. pseudosolanacearum*
617 in the presence of xylem carbon sources, we used the data and model generated in
618 Baroukh et al. (2024). In the study, a shake-flask growth experiment was performed in
619 a minimal medium supplemented with a mixture of organic substrates whose relative
620 concentrations mimics a tomato xylem. Growth, substrate assimilation and product
621 excretion were monitored and used to determine uptake, excretion and growth rates
622 among this combination of carbon sources. Glutamine and glucose assimilation
623 followed Monod-type kinetics and were driving growth, while other substrate
624 assimilation rates were proportional to the assimilation of glutamine and glucose. From
625 the Monod kinetics, two maximal assimilation rates, one for glutamine and one for
626 glucose, were implemented as a constraint bound in the model:

627 $$Gln_{ass_{rate}} \leq k_{gln} * \mu_{max_{gln}} * \frac{[Gln]}{[Gln] + K_{s_{gln}}} * 1000 * 24$$

628 $$Gluc_{ass_{rate}} \leq k_{gluc} * \mu_{max_{gluc}} * \frac{[Gluc]}{[Gluc] + K_{s_{gluc}}} * 1000 * 24$$

629 With:

630 - $Gln_{ass_{rate}}$ the assimilation rate of glutamine in the model (mmol·gB^{-1}·day^{-1}), k_{gln}
631 (mmol·mgB^{-1}) the quantity of glutamine necessary to yield 1mg of biomass,
632 $\mu_{\max_{gln}}$ (h^{-1}) the maximal growth rate on glutamine, $K_{S_{gln}}$ (mM) the semi-

633 saturation growth term on glutamine, $[Gln]$ (mM) the concentration of glutamine
634 in tomato xylem sap as measured in Gerlin et al. (2021)

635 • $Gluc_{ass_{rate}}$ the assimilation rate of glucose in the model (mmol·gB^{-1}·day^{-1}), k_{gluc}
636 (mmol·mgB^{-1}) the quantity of glucose necessary to yield 1g of biomass, $\mu_{\max_{gluc}}$
637 (h^{-1}) the maximal growth rate on glucose, $K_{S_{gluc}}$ (mM) the semi-saturation
638 growth term on glucose, $[Gluc]$ (mM) the concentration of glucose in tomato
639 xylem sap as measured in Gerlin et al. (2021)

640 From all the other substrates, to ensure assimilation only when glucose or glutamine
641 were assimilated, a constraint proportional to glucose and glutamine rate was added:

642 $$os_{ass_{rate}} \leq \frac{k_{OS}}{k_{gln}} * Gln_{ass_{rate}} + \frac{k_{OS}}{k_{gluc}} * Gluc_{ass_{rate}}$$

643 With $os_{ass_{rate}}$ (mmol·gB^{-1}·day^{-1}) the assimilation rate of the other substrate
644 (phenylalanine, valine, leucine, arginine, sucrose, tyrosine, proline, lysine, threonine,
645 isoleucine, asparagine). All values were taken from Baroukh et al. (2024).

646 The growth-associated and non-growth associated ATP maintenance terms were
647 calibrated so that *R. pseudosolanacearum* growth rate prediction was in agreement
648 with experimental data measured in Baroukh et al. (2024).

649 Sequential FBAs

650 Modeling of the pathosystem was performed using four successive FBAs with different
651 objective functions.

652 1. Minimization of photon uptake

653 This first FBA was performed on the plant alone. It minimized photon uptake while leaf,
654 stem and root growth rates were constrained to their experimental values taken from
655 Gerlin et al. (2022). Minimizing photon uptake allowed to estimate the physiological
656 capacities (photosynthesis, iron, nitrogen uptake) of a healthy plant.

657 2. Maximization of the pathogen growth

658 The second FBA was performed on the plant-pathogen model. It maximized the
659 pathogen biomass growth while the photon uptake rate was constrained to the value
660 found in FBA 1 (representing healthy plant photosynthetic capacities). This constraint
661 avoided to have an infected plant with a higher photosynthesis rate than a healthy
662 plant. The leaf and stem growth rates were relaxed, to model the fact that *R.*

663 *pseudosolanacearum* resource acquisition and proliferation can hinder the growth of
664 the aerial part, as observed experimentally (Gerlin, Escourrou, et al., 2021). Root
665 growth rate remained constrained as it was found experimentally that root growth was
666 not impacted by *R. pseudosolanacearum* presence (Gerlin, Escourrou, et al., 2021).

667 In this FBA, nitrogen or iron uptake rate could also be constrained to the ones of a
668 healthy plant as found in FBA 1. Transpiration rate of the plant could also be
669 constrained. Indeed, measurements of transpiration during tomato – *R.*
670 *pseudosolanacearum* interaction revealed a decrease of transpiration when the
671 pathogen is present at a density higher than 10^7 CFU per g of stem fresh weight (FW)
672 (Gerlin, Escourrou, et al., 2021). We estimated thanks to a linear regression the
673 following transpiration decrease linear rule:

674 $$\text{reduction_flow_coeff} = -0.2746 * [\log_{10} CFU.g^{-1} FW] + 2.8764.$$

675 As xylem fluxes of matter depend on the transpiration rate, the upper bound of each
676 flux exchanged between the root and the xylem ($v_{Exch_r_xyl_i}$) was constrained by the
677 value found in FBA1 ($vFBA1_{Exch_r_xyl_i}$) reduced by the reduction_flow_coeff, when the
678 bacterial density exceeded 10^7 $CFU.g^{-1}$ FW:

679 If $[\log_{10} CFU.g^{-1} FW] > 7$ then $v_{Exch_r_xyl_i} <= vFBA1_{Exch_r_xyl_i} *$ reduction_flow_coeff

680 3. Maximization of the growth of the aerial parts

681 The third FBA was performed on the plant-pathogen model. It maximized biomass
682 growth of the stem and the leaves of the plant, while the pathogen growth rate was
683 constrained to the value found in FBA 2. A constant ratio between leaf and stem
684 biomass was imposed to ensure balanced growth of both the stem and the leaves.
685 This FBA determined the growth of the aerial parts achievable in the presence of *R.*
686 *pseudosolanacearum*, since the pathogen used part of xylem nutrients.

687 4. Minimization of the sum of absolute fluxes

688 The fourth and final FBA was performed on the plant-pathogen model. It minimized the
689 sum of all fluxes of the model to ensure a parsimonious enzyme usage in both
690 organisms as well as avoid the presence of Stoichiometric Balanced Cycles. The leaf
691 and stem growth rates were constrained to the values found in FBA 3.

692 **Software requirements**

693 Simulations were performed with Python 3 scripts, the open access libraries lxml,
694 pandas and the linear programming solver CPLEX Python API, developed by IBM. The

scripts used to build the genome-scale metabolic models and perform all the simulations can be found on Github at this link: https://github.com/cbaroukh/VIRION.

An academic or commercial license of CPLEX Python API (ILOG CPLEX Optimization Studio) is mandatory to run the scripts. The academic license is free for academic institutions. The basic "free Community Edition" version of CPLEX is not suitable and will provide an error message.

Data availability

All data supporting the findings of this study are available within the paper and within its supplementary materials. The scripts used to perform all the simulations, as well as the genome-scale metabolic models, can be found on Github at this link: https://github.com/cbaroukh/VIRION.

Author contributions

Caroline Baroukh: Conceptualization (lead); Data curation (equal); Formal analysis (equal); Funding acquisition (lead); Investigation (equal); Methodology (equal); Project administration (lead); Resources (equal); Supervision (lead); Writing – original draft (supporting); Writing – review and editing (equal).

Léo Gerlin: Data curation (equal); Formal analysis (equal); Methodology (equal); Investigation (equal); Writing – original draft (lead); Writing – review and editing (equal).

Stéphane Genin: Conceptualization (supporting); Methodology (supporting); Resources (equal); Writing – review and editing (equal).

Competing interest statement

The authors declare no competing interests.

Funding statement

Léo Gerlin was funded by a PhD grant from the French Ministry of National Education and Research. The study was funded by the French Laboratory of Excellence (LABEX) project TULIP (ANR-10-LABX-41 and ANR11-IDEX-0002-02). The funders had no role in study design, data collection and analysis, decision to publish, or preparation of the manuscript.

724 ## Supplementary data

725 **Supplementary Figure 1**

726 *R. pseudosolanacearum* uptake rates depending on the bacterial density and the
727 limiting factors. g: g of *R. pseudosolanacearum* dry weight. CFU: colony forming units.

728 **Supplementary Text 1**

729 Modifications of tomato metabolic model to build a whole plant – pathogen model.

730 **Supplementary Text 2**

731 Integration of bacterial density in VIRION.

732

References

Abu Kwaik, Y., & Bumann, D. (2013). Microbial quest for food *in vivo* : 'Nutritional virulence' as an emerging paradigm: Microbial nutritional virulence. *Cellular Microbiology*, *15*(6), 882-890. https://doi.org/10.1111/cmi.12138

Baroukh, C., Gerlin, L., Escourrou, A., & Genin, S. (2025). Unraveling the in planta population dynamics of the plant pathogen Ralstonia pseudosolanacearum by mathematical modeling. *New Phytologist*, *246*(1), 251-261. https://doi.org/10.1111/nph.20216

Baroukh, C., Zemouri, M., & Genin, S. (2022). Trophic preferences of the pathogen *Ralstonia solanacearum* and consequences on its growth in xylem sap. *MicrobiologyOpen*, *11*(1), e1240. https://doi.org/10.1002/mbo3.1240

Berger, S., Sinha, A. K., & Roitsch, T. (2007). Plant physiology meets phytopathology : Plant primary metabolism and plant pathogen interactions. *Journal of Experimental Botany*, *58*(15-16), 4019-4026. https://doi.org/10.1093/jxb/erm298

Bhatt, G., & Denny, T. P. (2004). *Ralstonia solanacearum* Iron Scavenging by the Siderophore Staphyloferrin B Is Controlled by PhcA, the Global Virulence Regulator. *Journal of Bacteriology*, *186*(23), 7896-7904. https://doi.org/10.1128/JB.186.23.7896-7904.2004

Bialczyk, J., Lechowski, Z., & Dziga, D. (2004). Composition of the xylem sap of tomato seedlings cultivated on media with HCO_3^- and nitrogen source as NO_3 <sup/>—Or NH_4^+. *Plant and Soil*, *263*(1), 265-272. https://doi.org/10.1023/B:PLSO.0000047739.11698.ca

Dalsing, B. L., & Allen, C. (2014). Nitrate Assimilation Contributes to Ralstonia solanacearum Root Attachment, Stem Colonization, and Virulence. *Journal of Bacteriology*, *196*(5), 949-960. https://doi.org/10.1128/JB.01378-13

Dalsing, B. L., Truchon, A. N., Gonzalez-Orta, E. T., Milling, A. S., & Allen, C. (2015). Ralstonia solanacearum Uses Inorganic Nitrogen Metabolism for Virulence, ATP Production, and Detoxification in the Oxygen-Limited Host Xylem Environment. *mBio*, *6*(2), e02471-14. https://doi.org/10.1128/mBio.02471-14

De La Fuente, L., Merfa, M. V., Cobine, P. A., & Coleman, J. J. (2022). Pathogen Adaptation to the Xylem Environment. *Annual Review of Phytopathology*, *60*(1), 163-186. https://doi.org/10.1146/annurev-phyto-021021-041716

DeFalco, T. A., & Zipfel, C. (2021). Molecular mechanisms of early plant pattern-triggered immune signaling. *Molecular Cell*, *81*(17), 3449-3467. https://doi.org/10.1016/j.molcel.2021.07.029

diCenzo, G. C., Tesi, M., Pfau, T., Mengoni, A., & Fondi, M. (2020). Genome-scale metabolic reconstruction of the symbiosis between a leguminous plant and a nitrogen-fixing bacterium. *Nature Communications*, *11*(1), 2574. https://doi.org/10.1038/s41467-020-16484-2

Gerlin, L., Baroukh, C., & Genin, S. (2021). Polyamines : Double agents in disease and plant immunity. *Trends in Plant Science*, *26*(10), 1061-1071. https://doi.org/10.1016/j.tplants.2021.05.007

Gerlin, L., Cottret, L., Cesbron, S., Taghouti, G., Jacques, M.-A., Genin, S., & Baroukh, C. (2020). Genome-Scale Investigation of the Metabolic Determinants Generating Bacterial Fastidious Growth. *mSystems*, *5*(2), e00698-19. https://doi.org/10.1128/mSystems.00698-19

Gerlin, L., Cottret, L., Escourrou, A., Genin, S., & Baroukh, C. (2022). A multi-organ metabolic model of tomato predicts plant responses to nutritional and genetic perturbations. *Plant Physiology*, *188*(3), 1709-1723. https://doi.org/10.1093/plphys/kiab548

Gerlin, L., Escourrou, A., Cassan, C., Maviane Macia, F., Peeters, N., Genin, S., & Baroukh, C. (2021). Unravelling physiological signatures of tomato bacterial wilt and xylem metabolites exploited by *Ralstonia solanacearum*. *Environmental Microbiology*, *23*(10), 5962-5978. https://doi.org/10.1111/1462-2920.15535

Gerlin, L., Frainay, C., Jourdan, F., Baroukh, C., & Prigent, S. (2021). Plant genome-scale metabolic networks. In *Advances in Botanical Research* (Vol. 98, p. 237-270). Elsevier. https://doi.org/10.1016/bs.abr.2020.09.021

Gu, C., Kim, G. B., Kim, W. J., Kim, H. U., & Lee, S. Y. (2019). Current status and applications of genome-scale metabolic models. *Genome Biology*, *20*(1), 121. https://doi.org/10.1186/s13059-019-1730-3

Hamilton, C. D., Steidl, O. R., MacIntyre, A. M., Hendrich, C. G., & Allen, C. (2021). *Ralstonia solanacearum* Depends on Catabolism of Myo-Inositol, Sucrose, and Trehalose for Virulence in an Infection Stage–Dependent Manner. *Molecular Plant-Microbe Interactions®*, *34*(6), 669-679. https://doi.org/10.1094/MPMI-10-20-0298-R

Herms, D. A., & Mattson, W. J. (1992). The Dilemma of Plants : To Grow or Defend. *The Quarterly Review of Biology*, *67*(3), 283-335. https://doi.org/10.1086/417659

Ingel, B., Caldwell, D., Duong, F., Parkinson, D., McCulloh, K., Iyer-Pascuzzi, A. S., McElrone, A., & Lowe Power, T. (2022). Revisiting the source of wilt symptoms : X-ray microcomputed tomography provides direct evidence that Ralstonia biomass clogs xylem vessels. *PhytoFrontiers™*, *2*(1), 41-51. https://doi.org/10.1094/PHYTOFR-06-21-0041-R

Ingel, B., Caldwell, D., Duong, F., Parkinson, D. Y., McCulloh, K. A., Iyer-Pascuzzi, A. S., McElrone, A. J., & Lowe-Power, T. M. (2022). Revisiting the Source of Wilt Symptoms : X-Ray Microcomputed Tomography Provides Direct Evidence That *Ralstonia* Biomass Clogs Xylem Vessels. *PhytoFrontiers™*, *2*(1), 41-51. https://doi.org/10.1094/PHYTOFR-06-21-0041-R

Jian, Y., Gong, D., Wang, Z., Liu, L., He, J., Han, X., & Tsuda, K. (2023). How plants manage pathogen infection. *EMBO Reports*, *25*(1), 31-44. https://doi.org/10.1038/s44319-023-00023-3

Lacrampe, N., Lugan, R., Dumont, D., Nicot, P. C., Lecompte, F., & Colombié, S. (2024). Modelling metabolic fluxes of tomato stems reveals that nitrogen shapes central metabolism for defence against *Botrytis cinerea*. *Journal of Experimental Botany*, *75*(13), 4093-4110. https://doi.org/10.1093/jxb/erae140

Landry, D., González-Fuente, M., Deslandes, L., & Peeters, N. (2020). The large, diverse, and robust arsenal of *Ralstonia solanacearum* type III effectors and their in planta functions. *Molecular Plant Pathology*, *21*(10), 1377-1388. https://doi.org/10.1111/mpp.12977

Liu, L., & Bockmayr, A. (2020). Regulatory dynamic enzyme-cost flux balance analysis : A unifying framework for constraint-based modeling. *Journal of Theoretical Biology*, *501*, 110317. https://doi.org/10.1016/j.jtbi.2020.110317

Lowe-Power, T. M., Hendrich, C. G., Von Roepenack-Lahaye, E., Li, B., Wu, D., Mitra, R., Dalsing, B. L., Ricca, P., Naidoo, J., Cook, D., Jancewicz, A., Masson, P., Thomma,

825 B., Lahaye, T., Michael, A. J., & Allen, C. (2018). Metabolomics of tomato xylem sap
826 during bacterial wilt reveals *Ralstonia solanacearum* produces abundant putrescine, a
827 metabolite that accelerates wilt disease. *Environmental Microbiology*, *20*(4),
828 1330-1349. https://doi.org/10.1111/1462-2920.14020

829 Lowe-Power, T. M., Khokhani, D., & Allen, C. (2018). How Ralstonia solanacearum
830 Exploits and Thrives in the Flowing Plant Xylem Environment. *Trends in Microbiology*,
831 *26*(11), 929-942. https://doi.org/10.1016/j.tim.2018.06.002

832 Macho, A. P. (2016). Subversion of plant cellular functions by bacterial type- III
833 effectors : Beyond suppression of immunity. *New Phytologist*, *210*(1), 51-57.
834 https://doi.org/10.1111/nph.13605

835 MacIntyre, A. M., Barth, J. X., Pellitteri Hahn, M. C., Scarlett, C. O., Genin, S., & Allen,
836 C. (2020). Trehalose Synthesis Contributes to Osmotic Stress Tolerance and Virulence
837 of the Bacterial Wilt Pathogen *Ralstonia solanacearum*. *Molecular Plant-Microbe*
838 *Interactions®*, *33*(3), 462-473. https://doi.org/10.1094/MPMI-08-19-0218-R

839 Orth, J. D., Thiele, I., & Palsson, B. Ø. (2010). What is flux balance analysis? *Nature*
840 *Biotechnology*, *28*(3), 245-248. https://doi.org/10.1038/nbt.1614

841 Peyraud, R., Cottret, L., Marmiesse, L., & Genin, S. (2018). Control of primary
842 metabolism by a virulence regulatory network promotes robustness in a plant
843 pathogen. *Nature Communications*, *9*(1), 418. https://doi.org/10.1038/s41467-017-
844 02660-4

845 Peyraud, R., Cottret, L., Marmiesse, L., Gouzy, J., & Genin, S. (2016). A Resource
846 Allocation Trade-Off between Virulence and Proliferation Drives Metabolic Versatility
847 in the Plant Pathogen Ralstonia solanacearum. *PLoS Pathogens*, *12*(10), e1005939.
848 https://doi.org/10.1371/journal.ppat.1005939

849 Pfau, T., Christian, N., Masakapalli, S. K., Sweetlove, L. J., Poolman, M. G., &
850 Ebenhöh, O. (2018). The intertwined metabolism during symbiotic nitrogen fixation
851 elucidated by metabolic modelling. *Scientific Reports*, *8*(1), 12504.
852 https://doi.org/10.1038/s41598-018-30884-x

853 Rodenburg, S. Y. A., Seidl, M. F., Judelson, H. S., Vu, A. L., Govers, F., & De Ridder,
854 D. (2019). Metabolic Model of the *Phytophthora infestans* -Tomato Interaction Reveals
855 Metabolic Switches during Host Colonization. *mBio*, *10*(4), e00454-19.
856 https://doi.org/10.1128/mBio.00454-19

Roper, C., Castro, C., & Ingel, B. (2019). Xylella fastidiosa : Bacterial parasitism with hallmarks of commensalism. *Current Opinion in Plant Biology*, *50*, 140-147. https://doi.org/10.1016/j.pbi.2019.05.005

Thuillier, K., Baroukh, C., Bockmayr, A., Cottret, L., Paulevé, L., & Siegel, A. (2022). MERRIN: MEtabolic regulation rule INference from time series data. *Bioinformatics*, *38*(Supplement_2), ii127-ii133. https://doi.org/10.1093/bioinformatics/btac479

Vailleau, F., & Genin, S. (2023). *Ralstonia solanacearum* : An Arsenal of Virulence Strategies and Prospects for Resistance. *Annual Review of Phytopathology*, *61*(1), 25-47. https://doi.org/10.1146/annurev-phyto-021622-104551

Walters, D., & Heil, M. (2007). Costs and trade-offs associated with induced resistance. *Physiological and Molecular Plant Pathology*, *71*(1-3), 3-17. https://doi.org/10.1016/j.pmpp.2007.09.008

Yuan, H., Cheung, C. Y. M., Poolman, M. G., Hilbers, P. A. J., & Van Riel, N. A. W. (2016). A genome-scale metabolic network reconstruction of tomato (*Solanum lycopersicum* L.) and its application to photorespiratory metabolism. *The Plant Journal*, *85*(2), 289-304. https://doi.org/10.1111/tpj.13075

Zrimec, J., Correa, S., Zagorščak, M., Petek, M., Bleker, C., Stare, K., Schuy, C., Sonnewald, S., Gruden, K., & Nikoloski, Z. (2025). Evaluating plant growth–defense trade-offs by modeling the interaction between primary and secondary metabolism. *Proceedings of the National Academy of Sciences*, *122*(32), e2502160122. https://doi.org/10.1073/pnas.2502160122

Zupan, J., Muth, T. R., Draper, O., & Zambryski, P. (2000). The transfer of DNA from Agrobacterium tumefaciens into plants : A feast of fundamental insights. *Plant Journal*, *23*(1), 11-28. https://doi.org/10.1046/j.1365-313X.2000.00808.x

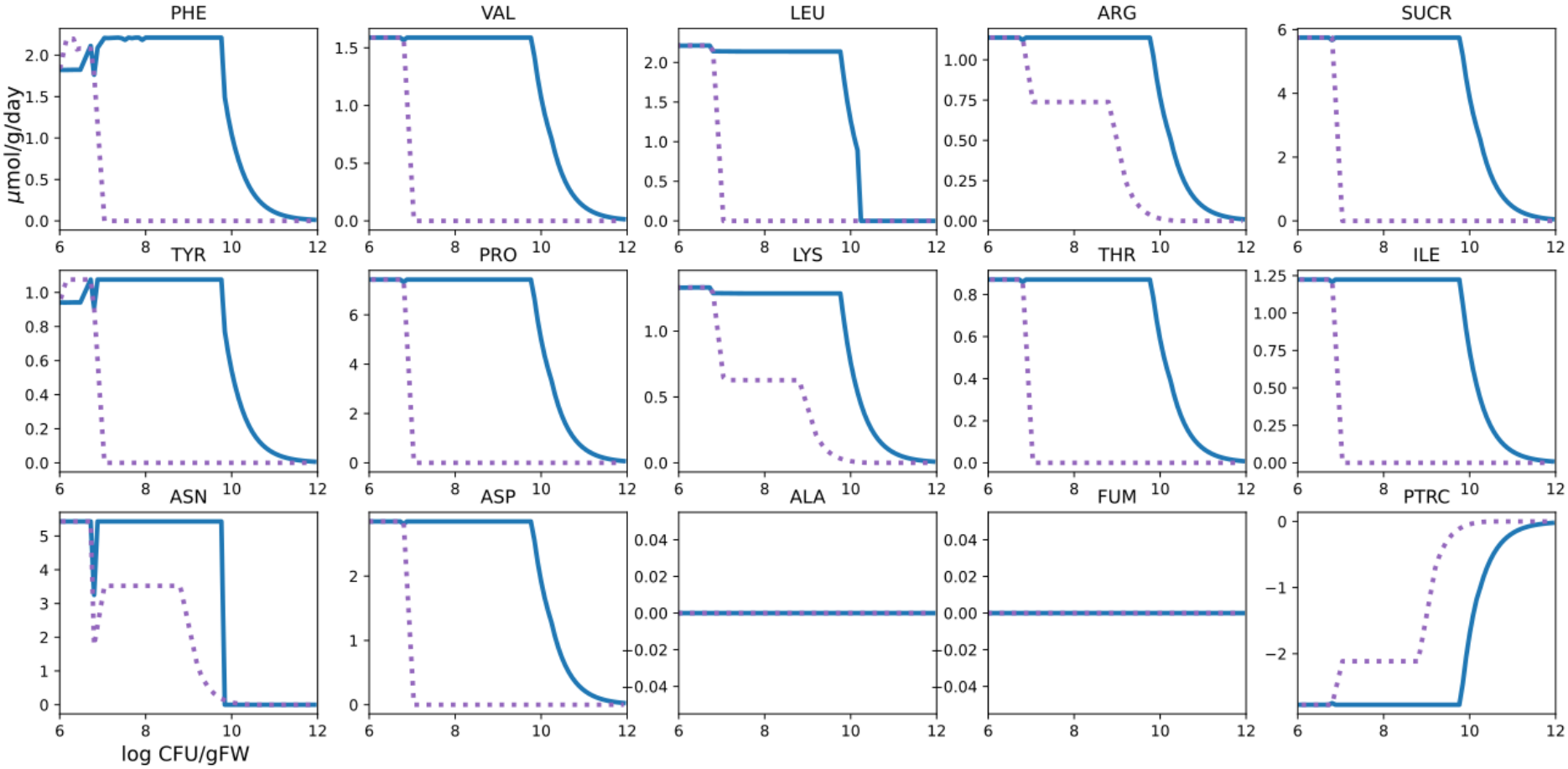

Supplementary figure 1: *R. pseudosolanacearum* uptake rates depending on the bacterial density and the limiting factors. g: g of *R. pseudosolanacearum* dry weight. CFU: colony forming units.

886 **Supplementary Table 1**

887 Experimental constraints used to calibrate the multi-organism metabolic model.

Variable	Constraint	Value	Note	References
leaf growth rate (day^{-1})	Lower bound	0.21		https://doi.org/10.1093/plphys/kiab548
stem growth rate (day^{-1})	Lower bound	0.26		https://doi.org/10.1093/plphys/kiab548
root growth rate (day^{-1})	Lower bound	0.17		https://doi.org/10.1093/plphys/kiab548
organic uptake, pathogen (mmol/g/day)	Upper bound	value in the macroscopic model of Ralstonia		https://doi.org/10.1111/nph.20216
pathogen:plant ratio (cells per g of plant fresh weight)	Stoichiometric coefficient between plant and xylem, and xylem and pathogen	10^6 - 10^{12}	Range of experimentally plausible values, based on experimental measurements	https://doi.org/10.1111/1462-2920.15535

transpiration reduction	Upper bound of 'root to xylem' exchange fluxes	*(-0.2746* [log_{10} CFU.g^{-1} FW] + 2.8764)* of uninfected root to xylem flux from FBA 1		https://doi.org/10.1111/1462-2920.15535
leaf:stem ratio (g/g)	Stoichiometric coefficient between leaf and stem biomass fluxes	2.2	To allow both leaf and stem biomass maximization in FBA 3	https://doi.org/10.1093/plphys/kiab548

888

Supplementary text 1

Modifications of tomato metabolic model to build a whole plant – pathogen model

1. Determination of iron concentration in tomato plant from literature for integration in biomass

Iron was initially absent from tomato biomass. Regarding its importance in plant – *Ralstonia* interaction (ref), we added it to organ biomass reactions (R_BIOMASS_ROOT, R_BIOMASS_STEM, R_BIOMASS_LEAF). We determined the coefficient value in the equation following the procedure below.

- **From Twyman, 1959 [1]**

Mean concentration of iron in dry leaf tissue of tomato plants:
[Fe] = 144 ppm at the highest iron supply (Table 2)
[Fe] = 144 ppm = 144 mg Fe/kg leaf DW

Note: at the lowest iron supply, the value remains close (112 mg Fe/kg leaf DW).

- **From Carpena et al., 1988 [2]**

Cultivar	Vermone	Marglobe
Nutrient consumption (mg Fe/plant) – Table 3	301	298
Yield, plant weight (g/plant) – Table 4	3054	2613
Yield, fruit weight (g/plant) – Table 4	6648	3930
Yield, plant dry weight (g DW/plant)*	432	370
Yield, fruit dry weight (g DW/plant)**	398	235
Total dry weight (g DW/plant)	830	605
Total dry weight (kg DW/plant)	0.830	0.733
[Fe] (mg Fe/kg DW)* **	**363**	**406.5**

*Using FW/DW ratio of 7.07 according to Gerlin et al., 2022 [3]

**Using FW/DW ratio of 16.7 (6% of dry content) [4]

***[Fe] (mg Fe/kg DW) = Nutrient consumption (mg Fe/plant)/Total dry weight (kg DW/plant)

➔ Integration of iron concentration in tomato model

The range estimated from literature is **144 – 406.5 mg Fe/kg DW** in a tomato plant.
Biomass equation represents 1 g of organ DW, corresponding to 1.44 – 4.07 10^{-4} g Fe.
Using the atomic weight of Fe (55.845 g/mol), it represents 2.58 – 7.28 10^{-6} mol Fe.
Biomass equation is expressed in µmol/gDW, so the range of values to integrate in the model is: **2.58 – 7.28 µmol/gDW.** Iron is majorly found in and between plant organs as Fe2+ (M_fe2_c) [5], so iron will be incorporated in biomass equation as M_fe2_c (see reference below).
Here, we do not take into account the organ specificity of iron concentration and add the same value in leaf, stem and root. We integrate the highest value to mimic a maximal requirement. Simulations presented in the paper show that even this high value has poor impact on the interaction.

2. Addition of minerals required for pathogen growth

Molybdate (M_mobd_c), manganese (M_mn_c) and cobalt (M_cobalt_c) are present in *R. pseudosolanacearum* biomass equation while they were not modeled in plant initial metabolic model (Sl2183).
We added:

- **For molybdate**

The internal metabolite M_mobd_c was already present. We added the boundary metabolite M_mobd_b and the uptake reaction R_EX_mobd_c, written as follow:
M_mobd_b <-> M_mobd_c

- **For manganese**

We added the internal and boundary metabolites M_mn2_b and M_mn2_c and the uptake reaction R_EX_mn2_c, written as follow:
M_mn2_b <-> M_mn2_c

- **For cobalt**

We added the internal and boundary metabolites M_cobalt2_b and M_cobalt2_c and the uptake reaction R_EX_cobalt2_c, written as follow:
M_ cobalt2_b <-> M_ cobalt2_c

3. Corrections of amino acid coefficients in biomass equation

The coefficients for some amino acids were inverted in the previous files of tomato model published in 2022 [3]. While it does not have significant impact on the simulations, either here or in the previous work, we rewrote the coefficients for the following amino acids: M_cys__L_c, M_ala__B_c, M_his__L_c, M_ile__L_c, M_leu__L_c, M_lys__L_c with the correct values from the list of biomass components (Supp File 1 of Gerlin et al. 2022 [3], sheets 3, 4, 5).

4. Putrescine metabolism

We manually examined putrescine catabolism in Sl2183, as our initial model was not representing putrescine catabolism. We looked at canonical putrescine catabolism in plants in literature [6] and databases (https://pmn.plantcyc.org/pathway?orgid=ARA&id=PWY-2).
We found that the first reaction of putrescine catabolism, putrescine oxidase* (EC 1.4.3.10) was already included in our model (converting putrescine into 4-aminobutanoate), but we missed the following reaction, aminobutyraldehyde dehydrogenase** (EC 1.2.1.19), converting 4-aminobutanoate into GABA. We found two orthologs (SOLYC06G071290 OR SOLYC03G113800) to the A. thaliana gene (ALDH10A9 / AT3G48170) annotated as aminobutyraldehyde dehydrogenase in BioCyc. This provides evidence for the completeness of the pathway in tomato, and we thus added aminobutyraldehyde dehydrogenase in the modeL

*Putrescine oxidase
R_PTRCOX1 http://bigg.ucsd.edu/universal/reactions/PTRCOX1 in BiGG
PUTRESCINE-OXIDASE-RXN https://biocyc.org/reaction?orgid=META&id=PUTRESCINE-OXIDASE-RXN in BioCyc
Reaction in BiGG: M_h2o_c + M_o2_c + M_ptrc_c -> M_4abutn_c + M_h2o2_c + M_nh4_c

**Aminobutyraldehyde dehydrogenase
R_ABUTD http://bigg.ucsd.edu/models/iJO1366/reactions/ABUTD in BiGG
AMINOBUTDEHYDROG-RXN https://biocyc.org/reaction?orgid=META&id=AMINOBUTDEHYDROG-RXN in BioCyc
Reaction in BiGG: M_4abutn_c + M_h2o_c + M_nad_c -> M_4abut_c + 2.0 M_h_c + M_nadh_c

References

[1] E. S. Twyman, « The effect of iron supply on the yield and composition of leaves of tomato plants », *Plant Soil*, vol. 10, nº 4, p. 375-388, avr. 1959, doi: 10.1007/BF01666211.
[2] O. Carpena, A. Masaguer, et M. J. Sarro, « Nutrient uptake by two cultivars of tomato plants », *Plant Soil*, vol. 105, nº 2, p. 294-296, sept. 1988, doi: 10.1007/BF02376796.
[3] L. Gerlin, L. Cottret, A. Escourrou, S. Genin, et C. Baroukh, « A multi-organ metabolic model of tomato predicts plant responses to nutritional and genetic perturbations », *Plant Physiol.*, vol. 188, nº 3, p. 1709-1723, mars 2022, doi: 10.1093/plphys/kiab548.
[4] E. Cozzolino *et al.*, « Effects of the Application of a Plant-Based Compost on Yield and Quality of Industrial Tomato (Solanum lycopersicum L.) Grown in Different Soils », *Appl. Sci.*, vol. 13, nº 14, p. 8401, juill. 2023, doi: 10.3390/app13148401.
[5] J.-F. Briat, C. Curie, et F. Gaymard, « Iron utilization and metabolism in plants », *Curr. Opin. Plant Biol.*, vol. 10, nº 3, p. 276-282, juin 2007, doi: 10.1016/j.pbi.2007.04.003.
[6] R. Rastogi et P. J. Davies, « Polyamine Metabolism in Ripening Tomato Fruit 1: I. Identification of Metabolites of Putrescine and Spermidine », *Plant Physiol.*, vol. 94, nº 3, p. 1449-1455, nov. 1990, doi: 10.1104/pp.94.3.1449.

Supplementary Text 2

Integration of bacterial density in VIRION

Numerical values used

$1.0157 \cdot 10^{12}$ CFU *Rs*/L = 1 OD	Value from (Peyraud et al., 2016) Linear regression from S4 Table.
0.414 g *Rs*/L = 1 OD	Value from (Peyraud et al., 2016) Materials and Methods.
g fresh weight / g dry weight [*Sl* stem] = 17.7	Value from (Gerlin et al., 2022) Figure 2.

g / CFU [*Rs*] = 0.414 g *Rs*/L / $1.0157 \cdot 10^{12}$ CFU *Rs*/L = $4.076 \cdot 10^{-13}$

1 cfu/g stem FW = 1·(g fresh weight / g dry weight [*Sl* stem]) = 17.7 **cfu/g stem DW**

In VYTOP model, the relative proportions are: 1.52 g stem DW and 3.37 g leaf DW for 1 g root DW. The bacterial density must be determined for 1.52 g stem DW.

1 cfu/g stem FW = 1.52 · 17.7 **cfu/1.52 g stem DW** = 26.904 **cfu/1.52 g stem DW**
1 cfu/g stem FW = 26.904 · (g / CFU [*Rs*]) **g bact / 1.52 g stem DW**
1 cfu/g stem FW = $26.904 \cdot 4.076.10^{-13}$ **g bact / 1.52 g stem DW**
1 cfu/g stem FW = $1.10 \cdot 10^{-11}$ **g bact / 1.52 g stem DW**

Rs: *Ralstonia pseudosolanacearum* GMI1000
Sl: *Solanum lycopersicum* M80

References

Peyraud R, Cottret L, Marmiesse L, Gouzy J, Genin S. A Resource Allocation Trade-Off between Virulence and Proliferation Drives Metabolic Versatility in the Plant Pathogen Ralstonia solanacearum. PLoS Pathog. 2016 Oct 12;12(10):e1005939. doi: 10.1371/journal.ppat.1005939. PMID: 27732672; PMCID: PMC5061431.

Gerlin L, Cottret L, Escourrou A, Genin S, Baroukh C. A multi-organ metabolic model of tomato predicts plant responses to nutritional and genetic perturbations. Plant Physiol. 2022 Mar 4;188(3):1709-1723. doi: 10.1093/plphys/kiab548. PMID: 34907432; PMCID: PMC8896645.